HT2023-107422

USE OF A GENETIC ALGORITHM TO MODEL THE INTERACTION OF CONDUCTION AND NUCLEATE BOILING MECHANISMS DURING EVAPORATION OF WATER DROPLETS ON SUPERHEATED ZNO NANOSTRUCTURED SURFACES

Anisa D. Silva and Van P. Carey

Mechanical Engineering Department University of California, Berkeley, CA

ABSTRACT

At low surface superheat levels, water droplets deposited on ZnO nanostructured surfaces vaporize primarily by conduction transport of heat from the solid heated surface to the liquid-vapor interface. As the superheat is increased beyond the onset of bubble nucleation threshold (ONB), an increasing number of active nucleation sites are observed within the evaporating droplet reducing the time required to completely evaporate the droplet. There were two primary objectives of this investigation; first, to determine how system parameters dictate when ONB occurs and how its heat transfer enhancement effect increases with superheat. The second was to develop a physics-inspired model equation for the evaporation time of a droplet on a nanostructured surface which accounts for effects of conduction transport in the liquid layer of the droplet and nucleate boiling.

A shape factor model for conduction-dominated vaporization of the droplet was first constructed. A correction factor was introduced to account for deviation of the measured droplet evaporation times from the conduction-dominated model. The correction factor form was postulated using a modified form of the onset of nucleate boiling parameter used in the well-known model analysis developed by Hsu to predict onset of nucleation and active nucleation site range in a thermal boundary layer associated with forced convection boiling. Droplet footprint radii were experimentally observed to be affected by superheat and an additional term was introduced to account for this phenomenon. A term was also introduced to include correlations for boiling to incorporate system properties.

This modeling led to an evaporation time equation containing numerical constants dictated by the idealizations from the physical modeling. To develop an improved empirical model equation, these numerical values were taken to be adjustable constants, and a genetic algorithm was used to determine the adjustable constant values that best fit a data collection spanning wide variations of droplet size, surface apparent contact angle, and superheat level. The best-fit constants match the data to an absolute fractional error of 26%. The model equation developed

in this study provides insight into the interaction between conduction transport and nucleate boiling effects that can arise in droplet vaporization processes.

Keywords: machine learning, droplet vaporization, nucleate boiling effects

NOMENCLATURE

Roman letters

d droplet footprint diameter

 D_b departure diameter

 h_{lv} latent heat of vaporization

 k_1 thermal conductivity of liquid

 \dot{q}_{mean} average rate of heat transfer

 $R_{s,0}$ initial droplet footprint radius

 $R_{s,mean}$ mean droplet footprint radius

 S_f shape factor

 t_e droplet evaporation time

f_e non-dimensional droplet evaporation time

 $\Delta T_{sat} = T_w - T_{sat}$ Surface superheat

 T_w heated wall temperature

 T_{sat} saturation temperature

 $V_{d,0}$ droplet volume

Greek letters

 α liquid thermal diffusivity

y Hsu's parameter

 $\delta_{mean,0}$ initial mean droplet height δ_{mean} process mean droplet height

 θ_{app}, θ apparent contact angle

 ρ_l liquid density

 ρ_v vapor density

 σ surface tension

 Ω boiling correlation

1. INTRODUCTION

Research has been done to investigate the increase in wickability and enhancement of droplet evaporation heat transfer

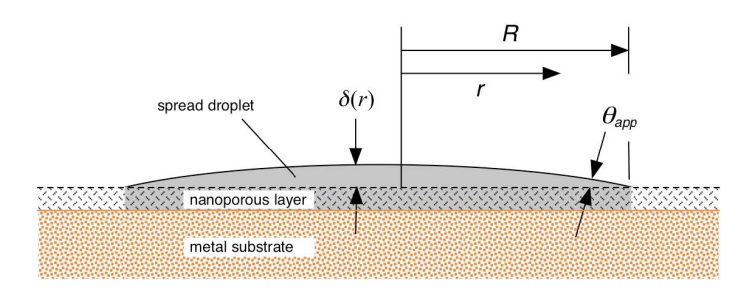


FIGURE 1: SEMI-SCHEMATIC DIAGRAM OF ENHANCED WICKING AND SPREADING ON A THIN NANOPOROUS LAYER ON A METAL SUBSTRATE DURING SYNCHRONOUS SPREADING [2].

through the use of nanostructured hydrophilic surfaces [1, 2], which shows promise in reducing water consumption where spray cooling methods are used. Two mechanisms exist that can potentially influence the vaporization rate of droplet deposition on superheated surfaces: conduction and nucleate boiling. However, little exploration has been completed on the interaction of these mechanisms on nanostructured surfaces. Contemporary research involving nanostructed surfaces has investigated: droplet evaporation at various superheat levels with each heat regime considered separately [3], nucleate boiling [4], and comparisons of the droplet evaporation and nucleate boiling [1]. The interactions of the droplet spreading mechanism and the mechanisms of heat transport to the interface of droplet on nanostructured hydrophilic surfaces has also been investigated [2].

ZnO nanostructured surfaces have been characterized as superhydrophillic which enables wettability and wickablity [5]. These mechanisms result in a two regime spreading process of synchronous and hemi-spreading of a deposited droplet onto the nanostructured surface. The spherical cap model uses the two regimes as a basis for its formulation. Figure 1 depicts the deposition of a droplet on a nanostructured surface at the transition point between synchronous and hemi-spreading. This transition point is of note in this research as it is when measurements are taken for the formulation of the apparent contact angle.

This paper will explore the interaction of conduction and nucleate boiling regimes of droplet vaporization from zinc oxide nanostructured surfaces and will investigate a physical model to encompass the droplet vaporization time as it crosses both regimes. To accomplish this, ZnO nanostructured surfaces were fabricated and experiments were completed to gather droplet vaporization data. Physical models were postulated based on ongoing and prior research. The two were then synthesized through the use of machine learning tools to hone in on a best fit physical model for the droplet evaporation process.

2. EXPERIMENTAL PROCEDURE AND RESULTS

Preliminary research work included fabrication and experimentation of the ZnO nanostructured surfaces and droplet evaporation. The fabrication and experimental procedure was first developed by Padilla, further explored and refined by Wemp and McClure, and has also been adapted to other applications by Cabrera [6–9]. The historical use of the fabrication and experimental techniques demonstrate the robustness of the procedure.

Based on the work done by the previous researchers, copper

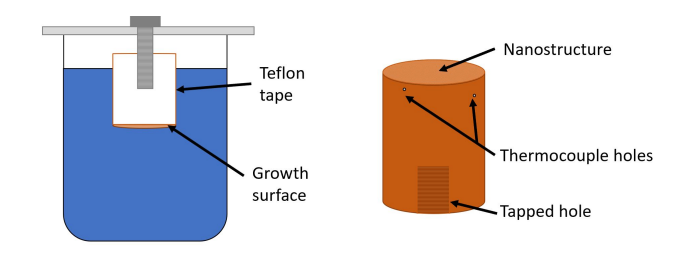


FIGURE 2: PICTORIAL REPRESENTATION OF SUBSTRATE WITH THE INITIAL NANOSTRUCTURE COATING AND THE BEAKER CONTAINING THE GROWTH SOLUTION WITH THE SUBSTRATE SUBMERGED [7].

was selected as the substrate material due to its favorable thermal properties. The goal of the experimental component of this research was to gather droplet evaporation time data to supplement the development of the physical and machine learning models which will be discussed later in this paper. In depth fabrication and experimental procedures can be found in the cited sources as modifications are minimal. Any differences in the referenced procedure will be outlined.

For all steps of the procedure (both fabrication and experimental), care was taken to handle the substrate and any materials used with gloves to prevent transfer of unwanted contaminates to the surfaces/substrate.

2.1 Fabrication

The general description of fabrication are to prepare the substrate followed by growing of the ZnO surface. For this experiment, an existing substrate was used to minimize fabrication times. The surface of the substrate where ZnO nanoparticles were to be grown was prepared by alternating sanding and alcohol cleaning steps until a homogeneous, mirror-finish was achieved. For each sanding step, sand paper grit size was reduced.

Following the preparation of the substrate surface, the substrate was then cleaned via an ultrasonic bath. The substrate was cleaned in successive baths of acetone, isopropyl alcohol, and finished with distilled water. A growth solution of distilled water, Hexamethylene Tetraamine, and Zinc Nitrate Hexahydrate was then prepared as described by Cabrera [6]. The nanoparticle solution was then prepared of the ZnO particles and ethanol which were exposed to ultrasonics to ensure mixture of the solution, again following the procedure as described by Cabrera [6]. Both of these processes create homogeneous solutions which promote uniform distribution and coating of the ZnO particles.

With the solutions and substrate prepared, fabrication proceeded with coating the surface with the nanoparticles and growing the nanostructure. The surface wass heated to 120°C, introduced to the nanoparticle solution, heated again, placed in a beaker of the growth solution, and the beaker was then placed in an oven for 8 hours at 90 °C to allow growth of the nanoparticles. Figure 2, shows the beaker with the substrate submerged; this is the configuration that was placed into the oven to enable nanoparticle growth.

Once the fabrication of the nanostructured surface and substrate was completed, the surface was imaged using an SEM to

gauge the success of the procedure and make any observations of the surface, Fig. 4. SEM images showed signature stochastic hexagonal pillars indicating a successful growth procedure.

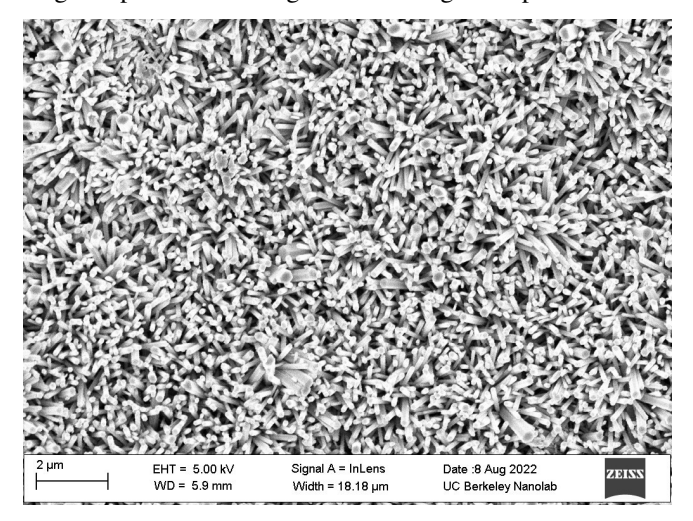


FIGURE 3: SEM IMAGE OF NANOSTRUCTURED SURFACE AT 2μm

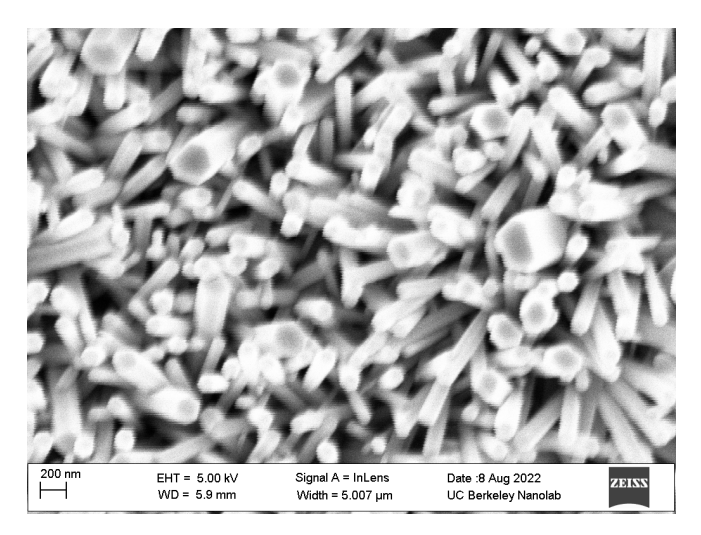


FIGURE 4: SEM IMAGE OF NANOSTRUCTURED SURFACE AT 200nm.

2.2 Experimental Procedure

The experimental component of the process included: desorption, characterization of the nanostructured surface, evaporation experiments, and post-processing.

2.2.1 Desorption. The surfaces were grown over the course of roughly 12 hours, therefore data gathering experiments took place a few days after growth procedures. Despite care to limit contamination, such as storing the substrate in clean glass containers, the lapse in time between growth and data gathering experiments could have resulted in unwanted contaminates on the nanostructured surface. To remove any unwanted contaminates, the substrate was desorbed. The desorption process was heating the substrate to 300 °C for about 45 minutes.

2.2.2 Characterization. Adiabatic droplet evaporation experiments were used to characterize the surface. The results of the characterization experiment were especially critical as it

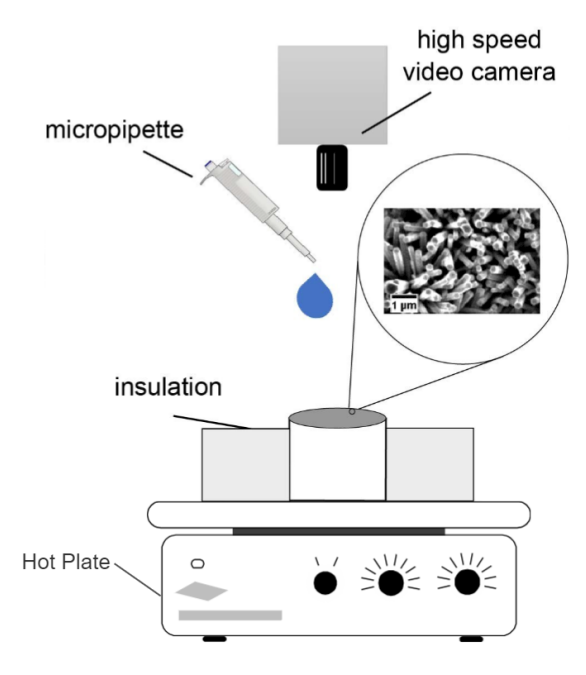


FIGURE 5: ADAPTED SCHEMATIC OF THE EXPERIMENTAL SET-UP WHERE A HOT-PLATE HAS BEEN ADDED TO THE DIAGRAM FOR COMPLETENESS, NOT TO SCALE [6].

provided data to calculate the contact angle of the surface which would be used throughout the remaining research. The test set-up was made up of the substrate, an Edgertronic high-speed camera, distilled water, and a pipette. Figure 5 demonstrates the experimental set-up for the adiabatic and heated experiments, where the only difference is the adiabatic experiments take place on an unheated hot plate. The high-level steps of the procedure as are as follows:

- 1. The high speed camera was set to capture video at 2000 fps
- 2. The substrate was placed directly beneath the camera lens.
- 3. The micropipette was filled to 8μ L of distilled water. The water is then deposited on the surface from a short distance. Simultaneously, the high speed camera captures a video of the deposition, spreading and evaporation process.

This process was repeated five times to generate several data points to ensure the contact angle generated was as accurate as possible. The videos were processed to gather footprint area measurements which will be outlined in the "Post-Processing" subsection.

2.2.3 Evaporation Experiments. Evaporation experiments closely followed those outlined in Cabrera's work [6]. The substrate was placed on the hot plate (see Fig. 5 in completeness) where it was then surrounded by insulation to mitigate heat loss from the sides of the substrate. A thermocouple was then carefully placed in the substrate via a pre-drilled hole; this would be used to control the temperature of the substrate. The hot plate was then set a few degrees above the desired temperature to ensure the substrate reached the desired temperature. Once the temperature was reached, about 15 minutes were allowed to pass to ensure

the system was at a steady state. An 8μ L droplet of distilled water was deposited at a negligible height from the surface and the droplet was vaporized. During this process, the camera captured a high speed video of the droplet deposition, spreading, and evaporation to later be analyzed.

This process was repeated at five superheat values with four to five runs at each superheat value for a total of 22 data points. Each experiment run used droplet volumes of $8\mu L$.

2.2.4 Post-Processing. The collection of videos from the surface characterization and evaporation experiments underwent two post processing procedures which utilized softwares Adobe Premier Pro and ImageJ. The desired output from the characteristic experiments was a foot print area which could then be used to calculate a contact angle and the desired output from the evaporation experiments were the droplet evaporation times.

The characteristic experiment videos were imported into Adobe Premier Pro where they were then analyzed to capture the transition of the droplet from synchronous spreading to hemispreading. An image was captured from the video frame just before hemi-spreading began. The form of the droplet here could then be used to calculate the contact angle as described in the introduction. The image captured was imported into ImageJ. The droplet area was measured using the ImageJ software tools and physical measurements of the substrate diameter as a scale. From the measurement of the droplet footprint area, the droplet radius was then calculated. The droplet is idealized as a spherical cap as developed by Wemp and Carey which assumes that a liquid droplet deposited on a substrate can be estimated as the cap of a sphere [5]. A relationship was developed between the initial droplet footprint radius, $R_{s,0}$, the apparent contact angle, θ_{app} , and the droplet volume, $V_{d,0}$:

$$R_{s,0} = \left(\frac{3V_{d,0}}{\pi(2 - 3cos(\theta_{app}) + cos^{3}(\theta_{app}))}\right)^{1/3} sin(\theta_{app}) \quad (1)$$

The footprint radius was measured and the droplet volume was known, from this relationship, the apparent contact angle was solved for.

Post-processing for the evaporation experiments was done in Adobe Premier Pro. For each experiment video, the video was imported into the software and scrubbed through to observe the frame in which the droplet first made contact with the substrate. This frame would then become the new start to the video. The time frame of the video was changed such that a time of 0s corresponded to when the droplet first met the surface. The video was the scrubbed again to find the frame in which the entirety of the droplet had vaporized and the frame was recorded. By converting the video time into frames, the evaporation time was then calculated. For example, a droplet was observed to have completely vaporized at a video time of 02:49:26, this converts to 5096 video frames, with a camera speed of 2000 fps, the evaporation time is then 2.548 seconds.

2.3 Results

2.3.1 Measurements. The contact angle was computed for each of the five adiabatic experiment replications using the relationship from Eq. 1. The values were averaged to get the contact angle of the surface, of 7.504° .

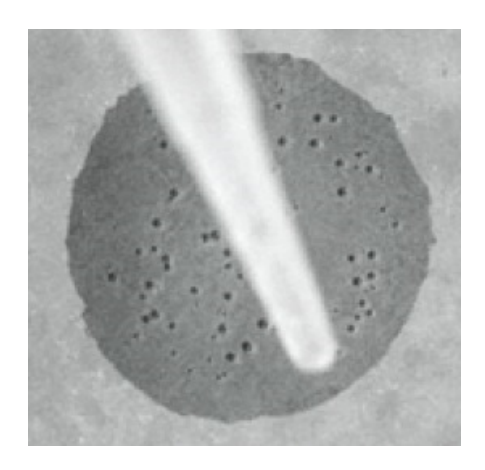


FIGURE 6: VIDEO IMAGE OF WATER DROPLET VAPORIZATION ON A NANOSTRUCTURED SURFACE WITH LOW SUPERHEAT NUCLEATE BOILING. SURFACE SUPERHEAT = 20°C.

2.4 Visual

Post-processing of the high speed videos yielded images of the two regimes of droplet vaporization. At 5°C superheat, the vaporization regime is postulated to be conduction dominated as it is below the general temperature range for the onset of nucleate boiling. Results of the experiments completed at this superheat confirm this hypothesis as the observed droplet contained a smooth appearance with no indication of nucleation sites. Similarly, between 15°C and 25°C it is estimated that the ONB will occur. In Fig. 6 the superheat is 20°C, and the ONB and nucleate boiling is observed. Research presented by Wemp also found similar results in which they observed no nucleate boiling at 15°C superheat and bubble nucleation at 20°C, indicating the onset of nucleate boiling occurs between these two superheat values [9].

3. MODEL DEVELOPMENT

3.1 Idealizations

Results from droplet evaporation experiments proved to loosely follow previously proposed physical models for predicting droplet evaporation. To improve upon the model proposed by Wemp [9], a closer look into the droplet evaporation time behavior with respect to the conduction regime was taken. As previously discussed, the droplet wicking in the ZnO nanostructured surfaces allows for more efficient conduction as the heat path has been shortened due to the height of the droplet decreasing with the wicking. The physical model followed an evolution based on continued analysis of mechanisms that best represent the physics of the droplet evaporation behavior.

To begin modeling droplet evaporation, a few assumptions were made that carried throughout the iterations on the physical model. As explained in the experimental procedure, the droplet is idealized as a spherical cap, the footprint radius can be measured, and the droplet volume is known, from this relationship, the apparent contact angle can be solved for, see Eq. 1. In order for the liquid droplet to vaporize, heat must transfer from the surface of the substrate across the liquid to interface. This is effectively heat transferring through the height of the droplet, δ . The initial mean droplet height $\delta_{mean,0}$ can be defined leveraging the spherical cap model and relating the footprint area, average

TABLE 1: LEGEND FOR 2-D PLOTS PRESENTED WITH heta ROUNDED TO THE NEAREST DEGREE

	$V_{d,0} = 4\mu L$	$V_{d,0} = 6\mu L$	$V_{d,0} = 8\mu L$	Source
$\theta = 5^{\circ}$		0	Δ	[7]
$\theta = 6^{\circ}$		•	<u> </u>	[7]
$\theta = 7^{\circ}$				[7]
$\theta = 8^{\circ}$				[7]
			A	This Study
$\theta = 9^{\circ}$				[7]
$\theta = 10^{\circ}$		0	Δ	[7]
$\theta = 11^{\circ}$ to 17°		0	Δ	[7]

droplet height, and the initial droplet volume:

$$\delta_{mean,0}(\pi R_{s,0}^2) = V_{d,0}$$

$$\delta_{mean,0} = \frac{V_{d,0}}{\pi R_{s,0}^2}$$
(2)

With the assumption of a fixed contact angle throughout the evaporation process, and as evaporation occurs, both the droplet volume and the mean droplet height both go to zero. The mean droplet height for the entire evaporation process can be idealized as:

$$\delta_{mean} = \frac{1}{2}(\delta_{mean,0} + 0) = \delta_{mean,0}/2 \tag{3}$$

A function $\lambda(\theta)$ is introduced to simplify the relationship between the droplet footprint radius, the contact angle, and the droplet volume:

$$\lambda(\theta) = \left(\frac{3sin^3(\theta_{app})}{\pi(2 - 3cos(\theta_{app}) + cos^3(\theta_{app}))}\right)^{1/3} \tag{4}$$

The initial droplet footprint radius, $R_{s,0}$, is reduced to the function $\lambda(\theta)$ and $V_{d,0}$. The relationships is then:

$$R_{s,0} = \lambda(\theta) V_{d,0}^{1/3} \tag{5}$$

Using the same logic as the formulation of the process mean droplet height (Eq. 2), a relationship for the average droplet footprint radius can be formed as:

$$R_{s,mean} = R_{s,0}/2 \tag{6}$$

Unless otherwise specified, these assumptions will carry throughout the physical model development to follow. The models and analysis in this paper span various contact angles and droplet volumes. A legend has been introduced in Table 1 for continuity and reference for plots presented.

3.2 Conduction Dominated Regime

An initial approach focused on the conduction transport dominated regime. A shape factor is introduced to best represent the hemispherical physical shape of the droplet on the surface. As developed by Nijaguna, and further simplified by Mendoza [10, 11], a shape factor for a hemispherical droplet can be formed as:

$$S_f = \frac{1}{4}\pi dsin\theta * \Phi(\theta) \tag{7}$$

Where $\Phi(\theta)$ is

$$\Phi(\theta) = \frac{4\left\{\sum_{n=0}^{\infty} \frac{(4n+3)(2n+1)(-1)^{2n}(2n!)^2}{(2n+2)^2(2)^{4n}(n!)^4}\right\}}{\left\{\sum_{n=0}^{\infty} \frac{(4n+3)(2n!)(-1)^n}{(2n+2)(2)^{2n}(n!)^2} \left[tan(\theta/2)\right]^{2n+1}\right\}}$$
(8)

The Nijaguna form of the shape factor was formulated using the droplet diameter. The focus for this study is the footprint of the droplet thus the sine term from the shape factor form is dropped resulting in:

$$S_f = \frac{1}{4}\pi d * \Phi(\theta) \tag{9}$$

The mean droplet footprint diameter, d, is defined as double the calculated mean footprint radius. The introduction of a shape factor allows for two- and three-dimensional heat conduction problems to be simplified by allowing the shape factor to encompass the geometry of the system [12]. The shape factor approach models heat transfer from the body of one surface to another - here the liquid-solid interface of the liquid water droplet at the surface to the liquid-gas interface of the droplet. The simplified the heat equation takes the form [12]:

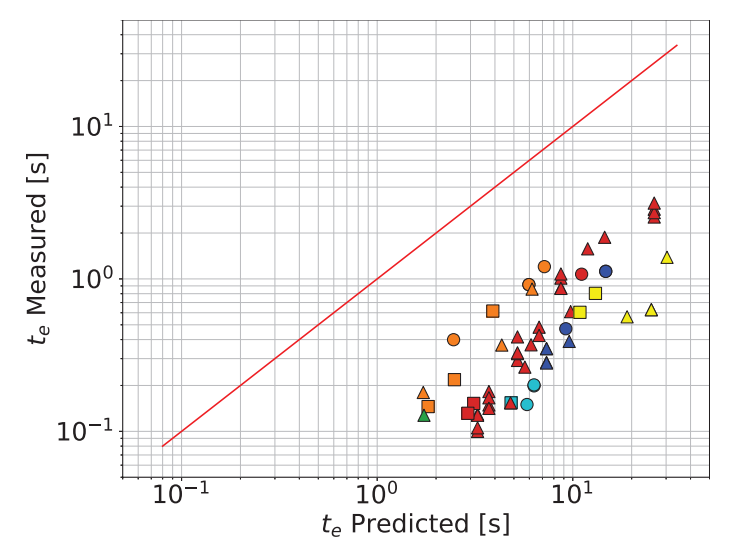
$$q = S_f k_l \Delta T_{sat} \tag{10}$$

Here k_l is the thermal conductivity of liquid water and $\Delta T_{sat} = T_{wall} - T_{sat}$ is the superheat, where the superheat can be defined as the difference in temperature of the heated surface and the saturation temperature of water. To develop a function for the droplet evaporation time, t_e , a relationship between the latent heat and the rate of heat transfer is established:

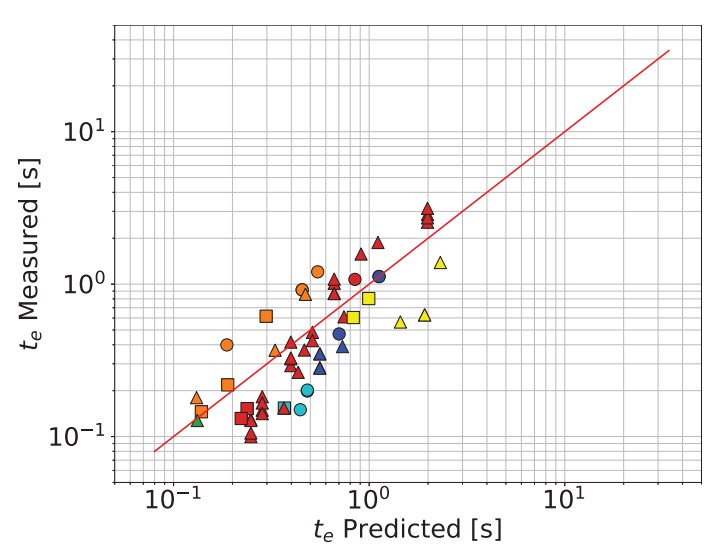
$$t_{e} = \frac{Q_{evap}}{\dot{q}_{mean}} = \frac{\rho_{l}h_{lv}V_{d,0}}{k_{l}S_{f}\Delta T_{sat}}$$

$$t_{e} = \frac{\rho_{l}h_{lv}V_{d,0}}{k_{l}\Delta T_{sat}} \left(\frac{1}{4}\pi d\Phi(\theta)\right)^{-1}$$
(11)

The droplet evaporation times were predicted using the developed shape factor model (Eq. 11) and compared to experimentally measured values, Fig. 7a. Visually, this plot demonstrates the general adherence of the predicted values where the conduction dominated regime is expected, at lower superheat values and thereby longer evaporation times. However, overall it is observed that the model predictions are below the red trendline of an exact prediction of evaporation times. The predicted evaporation times are shifted from the measured evaporation times due to the assumptions made, an unknown prefactor, and to the model only representing conduction-dominated evaporation regime.



(a) Shape Factor conduction model



(b) Corrected Shape Factor conduction model with n_1 prefactor for best

FIGURE 7: PREDICTIONS FROM THE SHAPE FACTOR CONDUC-TION DOMINATE REGIME MODEL, EQ. 11 (a) AND WITH THE AD-DITIONAL PREFACTOR (b), REFERENCE TABLE 1 FOR LEGEND.

A simple study was completed using a genetic algorithm to generate a best-fit value for this unknown prefactor; the section to follow will further discuss the use of genetic algorithms. A model following Eq. 11 was introduced to a genetic algorithm where a coefficient, which was allowed to float, was introduced, n_1 . The constant resulting in the predicted droplet evaporation times best fitting to the experimentally measured droplet evaporation times was found to be $n_1 = 0.0762$. A plot was generated using Eq. 11 with the addition of the constant, n_1 , to demonstrate the improvement of the addition of the "unknown" prefactor, see Fig. 7b. The immediate improvement of the fit in Fig. 7b is observed when compared to Fig. 7a, however, it can be seen that the higher superheat/shorter evaporation time values depart from the model. This departure can be attributed to the lack of inclusion of a nucleate boiling regime term in the model. It is expected that the correction prefactor will vary with superheat under the expectation that evaporation time will deviate increasingly from the conduction model as superheat increases and nucleation effects become stronger; a constant prefactor (n_1) is not sufficient.

3.3 Correction Term for Nucleate Boiling Effect

The predicted verses measured data plots for the conduction dominated regime model demonstrated a distinct departure from the model at shorter evaporation times. At higher superheat values evaporation times are expected to decrease. With this in mind, it can be deduced that the models until this point fairly accurately represented the actual behavior of droplet evaporation until around 15°C superheat. This can be attributed to the onset of nucleate boiling which was yet to be introduced to the postulated model. To account for the onset of nucleate boiling, an additional term was introduced to the model which would behave in a way such that at low values of superheat, the contribution of the term would be minimal to zero and at higher superheat values, the term would be significant.

The first approach for the addition of the nucleate boiling term followed the form of a Jakob number. As outlined in the previous paragraph, it was expected that as the system transitioned from conduction dominated heat transfer to nucleate boiling, the addition of the Jakob number would account for this transition. However, on analysis the term did not provide a good correlation scheme.

Following the proposed form including the Jakob number, the model was then refined by introducing the more appropriate form as found in Hsu's Analysis. Hsu's argument encompasses the nucleation site at which an embryo bubble would grow under the condition that the bubble is sufficiently large and in which its surroundings are sufficiently superheated [4]. Specifically, Hsu's analysis includes insight into mechanisms that impact the nucleation process [4]. This analysis includes a parameter, γ , of the form:

$$\gamma = \frac{12.8\sigma T_{sat}(P_l)}{\rho_v h_{lv} \delta_{mean} \Delta T_{sat}}$$
 (12)

Here the σ is the interfacial tension and T_{sat} is the saturation temperature. Hsu's analysis implies that the onset of nucleate boiling begins when this term is equal to one. With this in mind, the superheat necessary for the onset of nucleate boiling would take the form:

$$1 = \frac{12.8\sigma T_{sat}(P_l)}{\rho_v h_{lv} \delta_{mean} \Delta T_{ONB}}$$
 (13)

$$1 = \frac{12.8\sigma T_{sat}(P_l)}{\rho_v h_{lv} \delta_{mean} \Delta T_{ONB}}$$

$$\Delta T_{ONB} = (T_w - T_{sat})_{ONB} = \frac{12.8\sigma T_{sat}(P_l)}{\rho_v h_{lv} \delta_{mean}}$$

$$(13)$$

A beta term was then introduced to incorporate the parameter from Hsu's analysis where:

$$\beta_{ONB} = \frac{(T_w - T_{sat})}{(T_w - T_{sat})_{ONB}} \tag{15}$$

This formulation implies that when the system (numerator) is at a superheat below that required for the onset of nucleate boiling, β_{ONB} is less than one.

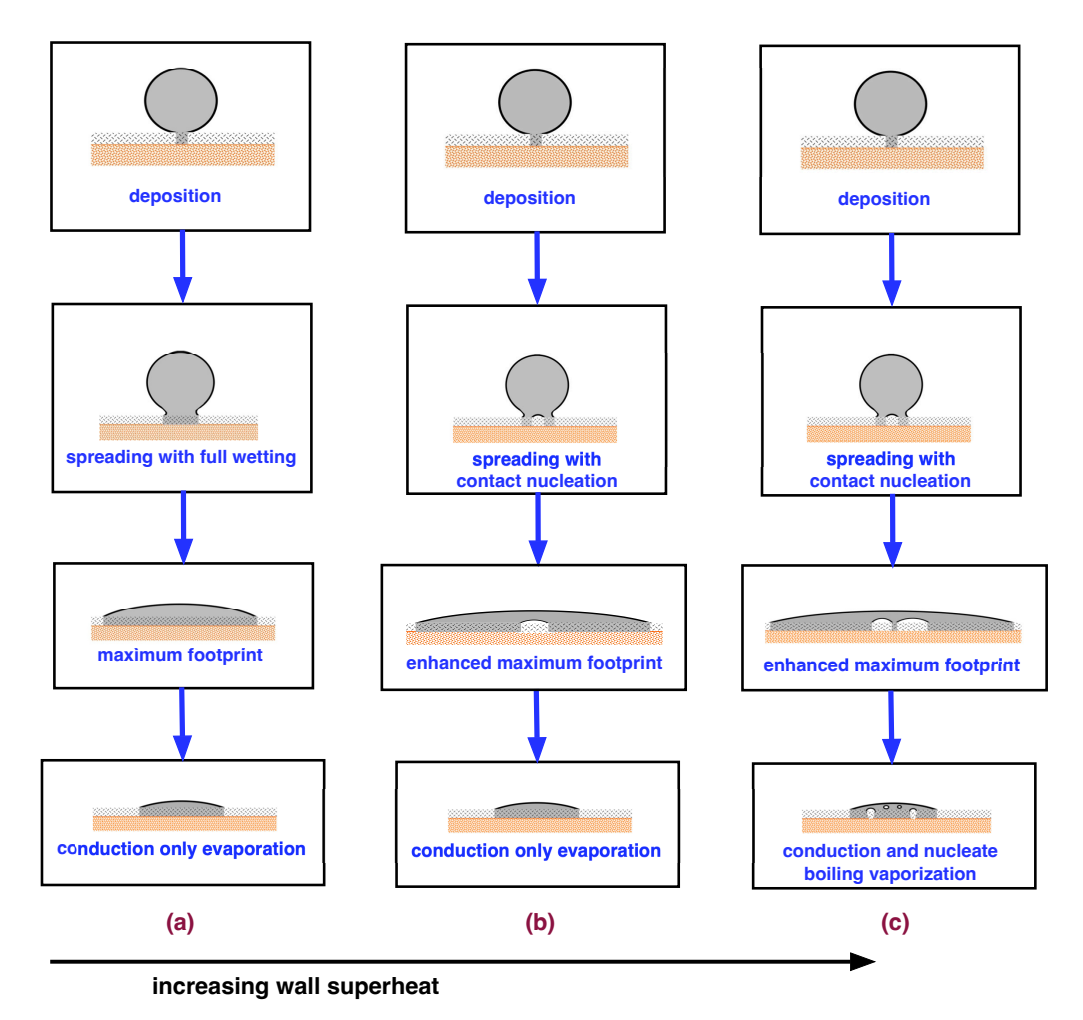


FIGURE 8: POTENTIAL INTERACTION OF MECHANISMS DURING DROPLET VAPORIZATION. (THICKNESS OF SURFACE COATING IS EXAGGERATED FOR CLARITY.) (A) CONDUCTION DRIVEN VAPORIZATION, (B) NUCLEATION ENHANCED SPREADING FOLLOWED BY CONDUCTION DOMINATED VAPORIZATION, (C) NUCLEATION ENHANCED SPREADING AND COMBINED CONDUCTION AND NUCLEATE BOILING VAPORIZATION

3.4 Non-Dimensional Form

A non-dimensional approach was then selected to remove reliance on the properties of the specific system used here. The non-dimensional form of the physical model is especially of interest because it would be most easily adapted to different systems as it is dimensionless and not reliant on system properties.

A non-dimensional form of the physical model for evaporation time was formulated to account for changes in the footprint radius with superheat. Post-processing of the experimental videos allowed for the maximum footprint radius to be measured through the measurement of the footprint area at each superheat used. Results of this analysis showed that the maximum footprint radius during adiabatic experiments differed significantly from that during heated experiments.

Figure 8 schematically illustrates the potential interaction of mechanism during deposited droplet vaporization on nanostructured surfaces. At very low superheat (a), droplets wet the surface fully, rapidly spread to a large footprint, and then evaporate as a consequence of conduction heat transfer across the spread liquid layer to the interface. At moderately high superheat levels (b), some nucleation and vaporization may occur when liquid first

contacts the surface. This vaporization can enhance spreading of the liquid to a larger footprint compared to very low superheat levels where this effect is not present.

The enhanced spreading will thin the liquid layer and enhance the rate of vaporization since there will be reduced conduction resistance across the liquid layer for the spread droplet. At this moderate superheat level, sustained nucleate boiling may not be achieved, and vaporization of the spread droplet is driven by conduction alone. At very high superheat levels, nucleation and vaporization occur when liquid first contacts the surface, and the superheat maybe high enough to sustain nucleate boiling in the liquid layer of the spread droplet, achieving a high vaporization rate as a consequence of the combined contributions of conduction across the liquid layer, and nucleate boiling at active nucleation sites in the liquid layer.

This lent itself to the formulation of a function to account for this phenomena. Leveraging previously defined relationships for the shape factor and $\lambda(\theta)$, Eq. 4, and defining a new function of superheat $F_s(\Delta T_{sat})$ as a correction term of maximum spreading radius due to nucleation, relationships for the maximum footprint radius and mean footprint radius including nucleation enhance-

ment are:

$$R_{s,max} = \lambda(\theta) V_{d,0}^{1/3} F_s \tag{16}$$

$$R_{s,mean} = \frac{1}{2}\lambda(\theta)V_{d,0}^{1/3}F_s$$
 (17)

following the same logic presented in the idealizations, Eq. 6. The droplet height can also be examined as it is a function of the footprint radius, Eq. 2. Using the form of maximum footprint radius defined above, Eq. 16, the equation for the initial mean droplet height and process mean droplet height become:

$$\delta_{mean,0} = \frac{V_{d,0}}{\pi R_{s,max}^2} = \frac{V_{d,0}}{\pi (\lambda(\theta) V_{d,0}^{1/3} F_s)^2} = \frac{V_{d,0}^{1/3}}{\pi \lambda^2(\theta) F_s^2}$$
(18)

$$\delta_{mean} = \frac{1}{2} (\delta_{mean} + 0) = \delta_{mean}/2 = \frac{V_{d,0}^{1/3}}{2\pi\lambda^2(\theta)F_s^2}$$
 (19)

The newly defined function F_s is proposed to take the form:

$$F_s = 1 + C_\beta \beta_{ONB}^{n_\beta} \tag{20}$$

where beta is that from Eq. 15. The function F_s is expected to approach 1 for $\Delta T_{sat} \leq (T_w - T_{sat})_{ONB}$. For the droplet at the onset condition superheat $(T_w - T_{sat})_{ONB}$ there is expected to be virtually no spreading enhanced by nucleation and $F_s = 1$. Therefore the initial and overall mean droplet height at the onset of nucleation are expected to take the form:

$$\delta_{mean,ONB,0} = \frac{V_{d,0}^{1/3}}{\pi \lambda^2(\theta)}$$
 (21)

$$\delta_{mean,ONB} = \frac{V_{d,0}^{1/3}}{2\pi\lambda^2(\theta)}$$
 (22)

The mean heat flux with possible enhancement of spreading by nucleation is:

$$q''_{cond,mean} = \frac{k_l S_f \Delta T_{sat}}{\pi R_{s,mean}^2} = \frac{k_l S_f \Delta T_{sat}}{(\pi/4)\lambda^2 (\theta) V_{s,0}^{2/3} F_s^2}$$
(23)

Here S_f is evaluated for the mean droplet footprint; $d=2R_{s,mean}$ is the mean diameter including nucleation enhancement. The total mean heat flux is represented by the combination of the conduction heat flux and fully developed nucleate boiling heat flux. A form of nucleate boiling heat flux was proposed by Stephan and Abdelsalam [13] and is represented by:

$$q'' = C_w \Delta T_{sat}^{3.07} \tag{24}$$

The coefficient C_w is represented by a function of contact angle, superheat, liquid/vapor properties, and departure diameter. This form of nucleate boiling heat flux utilizes correlations of nucleate boiling heat transfer data, specifically for natural convection boiling. Defining functions $\Omega(\theta)$ to account for contact angle dependence and D_b for departure diameter [14]:

$$\Omega(\theta) = \left(\frac{\rho_v}{\rho_l}\right)^{0.912} \left(\frac{h_{lv}D_b}{\alpha_l^2}\right)^{1.14} \left(\frac{\rho_l - \rho_v}{\rho_l}\right)^{-5.31} \left(\frac{\alpha_l^2 \rho_l}{\sigma D_b}\right)^{1.07} \tag{25}$$

$$D_b = 0.0208\theta \sqrt{\frac{\sigma}{g(\rho_l - \rho_v)}} \tag{26}$$

The coefficient, C_w , can then be defined as:

$$C_w = 0.011\Omega\left(\theta\right) \left(\frac{k_l T_{sat}}{D_b}\right) \left(\frac{1}{T_{sat}^{3.07}}\right) \tag{27}$$

With C_w defined, the total heat flux and total rate of heat transfer become:

$$q"_{tot,mean} = q"_{cond,mean} + q"_{nb,mean}$$

$$q"_{tot,mean} = \frac{k_l S_f \Delta T_{sat}}{(\pi/4)\lambda^2 (\theta) V_{d,0}^{2/3} F_s^2} + C_w \Delta T_{sat}^{3.07}$$
(28)

$$\dot{q}_{tot,mean} = q''_{tot,mean} \pi R_{s.mean}^{2}$$

$$= \frac{k_{l} S_{f} \Delta T_{sat} \pi R_{s.mean}^{2}}{(\pi/4) \lambda^{2}(\theta) V_{d.0}^{2/3} F_{s}^{2}} + C_{w} \pi R_{s.mean}^{2} \Delta T_{sat}^{3.07}$$
(29)

Evaporation time can then be solved for using the following relationship:

$$t_e = \frac{\rho_l h_{lv} V_{d,0}}{\dot{q}_{tot,mean}} \tag{30}$$

Non-dimensional time is defined as:

$$\hat{t}_e = \frac{t_e(\pi/4)\lambda(\theta)\Phi(\theta)}{\rho_l h_{lv} V_{d,0}^{2/3}/(k_l \Delta T_{sat})}$$
(31)

After substituting in values and simplification, the nondimensional model becomes:

$$\hat{t}_{e} = \frac{1}{F_{s} + \frac{C_{w}\lambda(\theta)F_{s}^{2}V_{d,0}^{1/3}\Delta T_{sat}^{n_{w}}}{\phi(\theta)k_{b}\Delta T_{cot}}}$$
(32)

The definition of C_w , Eq. 27, is then substituted in to further refine and simplify the physical model form of non-dimensional time:

$$\hat{t}_{e} = \left[F_{s} + 0.011 \left(\frac{V_{d,0}^{1/3} F_{s}^{2}}{D_{b}} \right) \left(\frac{\Omega\left(\theta\right) \lambda\left(\theta\right)}{\Phi\left(\theta\right)} \right) \left(\frac{\Delta T_{sat}}{T_{sat}} \right)^{2.07} \right]^{-1}$$
(33)

4. DROPLET EVAPORATION TIME USING MACHINE LEARNING

4.1 Genetic Algorithm Development

A genetic algorithm (GA) was selected as the machine learning tool as it was a straightforward transition from the physical model. By using the genetic algorithm, the form of the physical model was maintained allowing the model to be analyzed in a dimensional or non-dimensional form. Additionally, genetic algorithm framework has the capability to allow for non-linear functions. This feature is especially critical in the research presented here as the physical models developed became non-linear with successive iterations to best fit the physics of the vaporization process.

Generally, a genetic algorithm begins with a representative population of the process of interest, such as the data from the

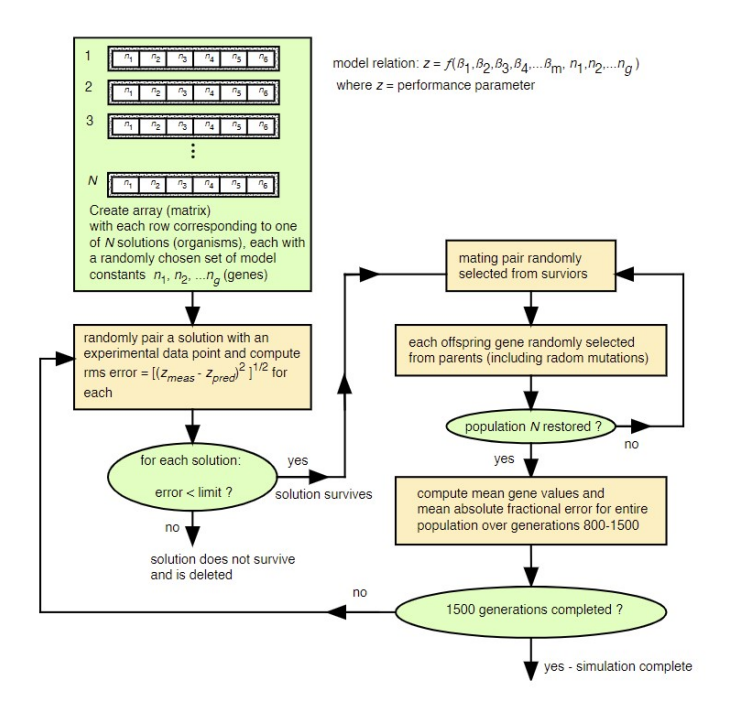


FIGURE 9: FLOW CHART OF AN EXAMPLE GENETIC ALGORITHM [15].

evaporation experiments. A fitness function is then determined; in this exploration it will be a form of each of the postulated physical models. Based off of the fitness function, the fittest individuals will be selected to pass their "genes" to the next generation. New "offspring" is generated from the pairing of two random "parents" which are then added to the population. Those individuals with low fitness are removed from the population, leaving only the fittest individuals. This process is repeated until satisfactory accuracy is achieved. See Fig. 9 for an example flow chart of the process. Main components of the genetic algorithm are the tuneable constants. The program works to minimize the error between the representative population and the value generated using the floating constants and selects constants that best accomplish that.

The purpose of the use of a genetic algorithm was to develop constants for the developed physical models. Because the physical models rely on idealizations, the constants are also reliant on the idealizations and may not generate the best fit for modeling the physical behavior. The genetic algorithm enabled the experimental data to fill-in the knowledge gaps about real world droplet evaporation. For each of the physical models developed, a genetic algorithm was run where results provided objective feedback on how the next iteration of the physical model could be improved. The genetic algorithm programs each used the experimental data gathered in the research done here and that of McClure [7].

4.2 Postulated Fits and Constants - Conduction and Nucleate Boiling

The non-dimensional physical model derived, includes a term to account for the onset of nucleate boiling which enables the model span the transition from conduction dominated heat transfer to nucleate boiling. This physical model was reformulated

TABLE 2: SUMMARY OF INITIAL GUESSES AND BEST FIT CONSTANTS FOR NON-DIMENSIONAL MODEL.

	C_{β}	n_{β}	C_{nb}	n_{nb}
Initial	1	2	0.011	2.07
Best Fit	5.059	0.677	0.013	12.309

to include adjustable constants in place of theoretical coefficients and exponential terms to allow the model to fit the experimental data. The floating constants introduced were mutated until the best fit was achieved based on an absolute error fraction:

$$Error = \left| \frac{\hat{t}_{e,exp} - \hat{t}_{e,pred}}{\hat{t}_{e,exp}} \right|$$
 (34)

4.2.1 Non-Dimensional Form. The developed form of non-dimensional time using the term from Hsu's analysis and terms for nucleate boiling correlation from Stephan and Abdelsalam was postulated as Eq. 35 where F_s is represented as Eq. 20.

$$\hat{t}_{e} = \left[F_{s} + C_{nb} \left(\frac{V_{d,0}^{1/3} F_{s}^{2}}{D_{b}} \right) \left(\frac{\Omega \left(\theta \right) \lambda \left(\theta \right)}{\Phi \left(\theta \right)} \right) \left(\frac{\Delta T_{sat}}{T_{sat}} \right)^{n_{nb}} \right]^{-1}$$
(35)

To leverage a GA the constants previously defined are allowed to float including those present in the F_s function. Explicitly the constants are: C_β , n_β , C_{nb} (previously 0.011), and n_{nb} (previously 2.07), each is dimensionless. The resulting mean fractional error from the GA was **0.2587** where the best-fit constants are those found in Table 2. The fit of the measured versus predicted non-dimensional evaporation times can be seen in Fig. 10. With the best-fit constants generated, Eq. 35 was updated to Eq. 37 with the updated constants. The resulting function with the best fit constants was then used to generate a surface plot, Fig. 11, where it can be seen that as the superheat goes to zero, \hat{t}_e approaches 1, which is expected.

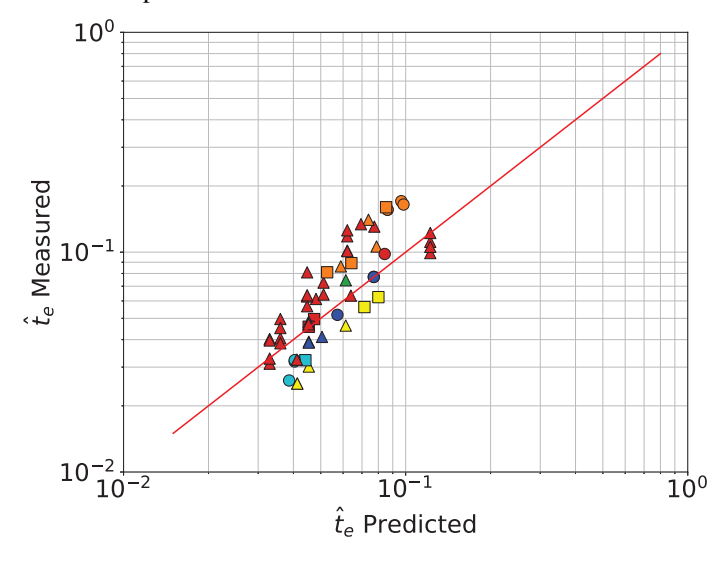


FIGURE 10: RELATIONSHIP BETWEEN EXPERIMENTALLY MEASURED NON-DIMENSIONAL EVAPORATION TIMES TO PREDICTED VALUES USING EQ. 37, REFERENCE TABLE 1 FOR LEGEND.

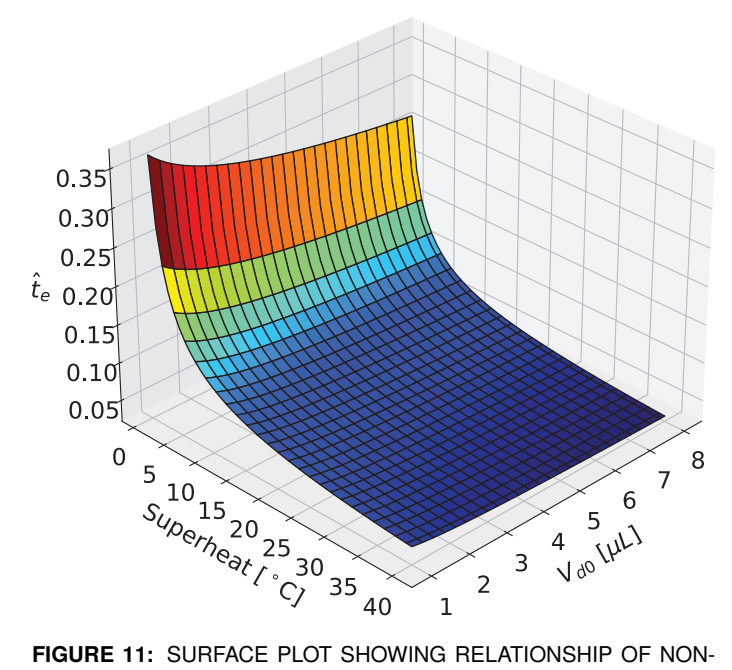


FIGURE 11: SURFACE PLOT SHOWING RELATIONSHIP OF NON-DIMENSIONAL TIME TO DROPLET VOLUME AND SUPERHEAT WITH $\theta=10^\circ$ FOR LIQUID WATER.

The postulated non-dimensional form showed good agreement with the experimental data. The bracketed term of Eq. 35 is equal to F_s if no nucleate boiling flux is present, and the equation becomes $\hat{t}_e = \frac{1}{F_s}$. It then follows that nucleate boiling effects turn on when the term in brackets in Eq. 35 is substantially larger than 1. Selecting a threshold as what is significantly different than 1 to be 0.15 (15% effect), the results here indicate the threshold condition for turning on of nucleate boiling is below in the form including F_s and a simplified form with the terms for F_s substituted in:

$$F_{s} + C_{nb} \left(\frac{V_{d,0}^{1/3} F_{s}^{2}}{D_{b}} \right) \left(\frac{\Omega\left(\theta\right) \lambda\left(\theta\right)}{\Phi\left(\theta\right)} \right) \left(\frac{\Delta T_{sat}}{T_{sat}} \right)^{n_{nb}} > 1.15$$

$$C_{\beta}\beta_{ONB}^{n_{\beta}} + C_{nb} \left(\frac{V_{d,0}^{1/3} F_{s}^{2}}{D_{b}} \right) \left(\frac{\Omega\left(\theta\right) \lambda\left(\theta\right)}{\Phi\left(\theta\right)} \right) \left(\frac{\Delta T_{sat}}{T_{sat}} \right)^{n_{nb}} > 0.15$$
(36b)

4.3 Discussion

The iterative process of working through the physical model development in tandem with the genetic algorithm development provided for an excellent opportunity to refine the postulated model with knowledge from experimental data. The resulting best fit postulated physical model for non-dimensional evaporation time is:

$$\hat{t}_{e} = \left[F_{s} + 0.013 \left(\frac{V_{d,0}^{1/3} F_{s}^{2}}{D_{b}} \right) \left(\frac{\Omega\left(\theta\right) \lambda\left(\theta\right)}{\Phi\left(\theta\right)} \right) \left(\frac{\Delta T_{sat}}{T_{sat}} \right)^{12.309} \right]^{-1}$$
(37a)

$$F_s = 1 + 5.059 \beta_{ONB}^{0.677} \tag{37b}$$

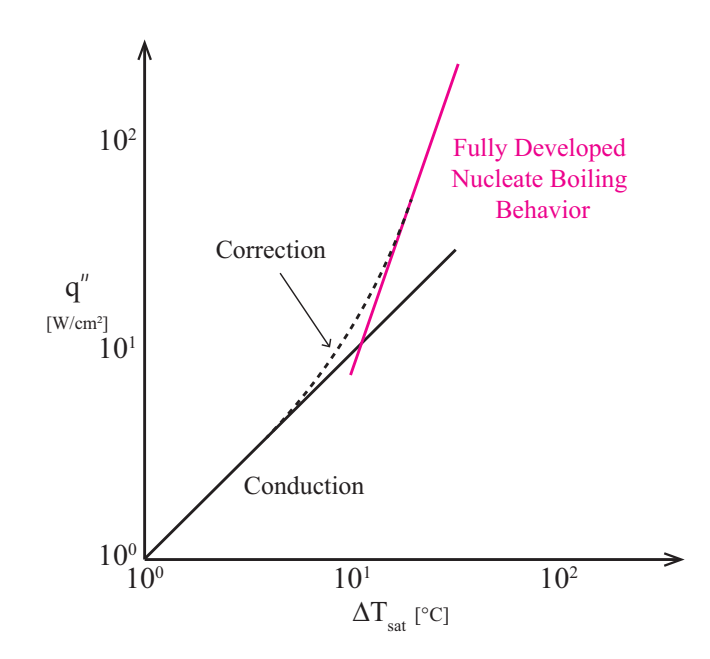


FIGURE 12: EXAMPLE BOILING CURVE FOR DROPLET BEHAVIOR.

where the floating constants have been replaced with the best-fit constants. With the best-fit constants generated, the proposed threshold for the onset of nucleate boiling, Eq. 36a, can be updated so that onset of nucleate boiling can be predicted to occur when:

$$5.059\beta_{ONB}^{0.677} + 0.013 \left(\frac{V_{d,0}^{1/3}F_s^2}{D_b}\right) \left(\frac{\Omega\left(\theta\right)\lambda\left(\theta\right)}{\Phi\left(\theta\right)}\right) \left(\frac{\Delta T_{sat}}{T_{sat}}\right)^{12.309} > 0.15$$

$$(38)$$

The non-dimensional form presented here generally follows a pool boiling curve. The introduced F_s function incorporates the linear behavior observed in conduction dominated heat transport at the low superheat range. In Fig. 12, the floating constant in the additional superheat term in the bracketed term of Eq. 33, $\Delta T_{sat}^{n_{nb}}$, has converged on a value which facilitates closing the gap between the conduction dominated regime and a more fully developed nucleate boiling process.

5. CONCLUSION

This exploration of water droplet evaporation heat transfer data for droplet evaporation from a nanoporous thin layer of ZnO pillars demonstrated the ability to encompass the conduction dominated and the nucleate boiling dominated regimes associated with the evaporation process. The effects of the onset of nucleate boiling evaporation process from the nanostructured surfaces were explored experimentally, visually demonstrating the range of where the onset of nucleate boiling takes place.

Various physical models were developed to represent the evaporation behavior from the ZnO nanostructured surfaces, beginning with a conduction dominated representation and continuing with the addition of a term to account for the onset of nucleate boiling, which took several forms as the machine learning tools allowed for refinement of the form selected. The physical models

then took a non-dimensional form where a correction term was introduced that accounted for the droplet spreading enhanced by bubble inflation and increased superheat values.

The model presented provides physically representative means for predicting where the transition from a conduction dominated regime to a nucleate boiling dominated regime occurs. The final form includes the two represented regimes as well as the correction term for enhanced droplet spreading. Key to this formulation was the inclusion of the term introduced in Hsu's analysis and expanding upon it for this application.

ACKNOWLEDGMENTS

Support for this research under NSF CBET grant number 2228373 was provided and is gratefully acknowledged.

REFERENCES

- [1] Cabrera, Samuel and Carey, Van P. "Comparison of Droplet Evaporation and Nucleate Boiling Mechanisms on Nanoporous Superhydrophilic Surfaces." *ASME 2019 Heat Transfer Summer Conference*. 2019. ASME, American Society of Mechanical Engineers, NEW YORK.
- [2] Carey, Van P, Wemp, Claire K, McClure, Emma R and Cabrera, Samuel. "Mechanism Interaction During Droplet Evaporation on Nanostructured Hydrophilic Surfaces." Volume 8A: Heat Transfer and Thermal Engineering. 2018. American Society of Mechanical Engineers.
- [3] Padilla, Jorge and Carey, Van P. "Water Droplet Vaporization on Superhydrophilic Nanostructured Surfaces at High and Low Superheat." Vol. Volume 8B: Heat Transfer and Thermal Engineering. 2014.
- [4] Carey, Van P. *Liquid-vapor phase-change phenomena*. CRC Press (2020): Chap. 6, p. 203–247.
- [5] Wemp, Claire K. and Carey, Van P. "Water Wicking and Droplet Spreading on Randomly Structured Thin Nanoporous Layers." *Langmuir* Vol. 33 (2017): pp. 14513–14525. DOI 10.1021/acs.langmuir.7b03687.
- [6] Cabrera, Samuel. "Fabrication and Testing of Zinc Oxide Superhydrophilic Nanostructured Surfaces on Metal Sub-

- strates and Wavy Fin Geometries for Use in Spray Cooling." Ph.D. Thesis, University of California, Berkeley. 2022.
- [7] McClure, Emma. "Zinc Oxide Nanoporous Superhydrophilic Surfaces: A Synthesis of Experimental Durability Testing and Droplet Vaporization Model Development Using Machine Learning Methods." Ph.D. Thesis, University of California, Berkeley. 2021.
- [8] Padilla, Jorge. "Experimental Study of Water Droplet Vaporization on Nanostructured Surfaces." Ph.D. Thesis, University of California, Berkeley. 2014.
- [9] Wemp, C.K. "An Exploration of Nanostructured Surfaces for Wicking and Vaporization Enhancement." Ph.D. Thesis, University of California, Berkeley. 2018.
- [10] Mendoza, Hector, Beaini, Sara and Carey, Van P. "An Exploration of Transport Within Microdroplet and Nanodroplet Clusters During Dropwise Condensation of Water on Nanostructured Surfaces." *Journal of heat transfer* Vol. 136 No. 12 (2014): pp. 121501–.
- [11] Nijaguna, B. T. "Drop Nusselt numbers in dropwise condensation." *Applied Scientific Research* Vol. 29 No. 1 (1974): pp. 226–236.
- [12] Bergman, T. L. and Incropera, Frank P. Fundamentals of heat and mass transfer. Wiley (2011).
- [13] Stephan, K. and Abdelsalam, M. "Heat-transfer correlations for natural convection boiling." *International Journal of Heat and Mass Transfer* Vol. 23 No. 1 (1980): pp. 73–87. DOI https://doi.org/10.1016/0017-9310(80)90140-4.
- [14] Ghiaasiaan, S. Mostafa. *Two-phase flow, boiling and condensation in conventional and miniature systems*. Cambridge University Press (2008): Chap. 11, p. 287–320.
- [15] Njike, Ursan Tchouteng, Cabrera, Samuel, McClure, Emma R. and Carey, Van P. "Use of Machine Learning Tools to Assess Surface Dryout During Nucleate and Transition Boiling on Surfaces With Different Wetting and Substrate Properties." Vol. ASME 2021 Heat Transfer Summer Conference. 2021. DOI 10.1115/HT2021-64012.